# Cold-Sintered Temperature Stable Na$_{0.5}$Bi$_{0.5}$MoO$_4$–Li$_2$MoO$_4$ Microwave Composite Ceramics

Dawei Wang,[*,†] Di Zhou,[†,§] Shiyu Zhang,[‡] Yiannis Vardaxoglou,[‡] Willian G Whittow,[‡] Darren Cadman,[‡] and Ian M. Reaney[*,†]

[†]Department of Materials Science and Engineering, University of Sheffield, Sheffield S1 3JD, United Kingdom

[‡]Wolfson School of Mechanical, Electrical and Manufacturing Engineering, Loughborough University, Loughborough LE11 3TU, United Kingdom

**ABSTRACT:** A cold sintering process (150 °C, 30 min and 200 MPa) was employed to fabricate Na$_{0.5}$Bi$_{0.5}$MoO$_4$–Li$_2$MoO$_4$ (NBMO-LMO) composites with up to 96.4% relative density. X-ray diffraction traces, backscattered electron images and Raman spectra indicated the coexistence of NBMO and LMO phases in all composites with no detectable secondary phases. The permittivity ($\varepsilon_r$) and temperature coefficient of resonant frequency (TCF) decreased, whereas microwave quality factor ($Q \times f$) increased, with increasing weight % LMO. Near-zero TCF was obtained for NBMO-20 wt %LMO with $\varepsilon_r \sim 17.4$ and $Q \times f \sim$ 7470 GHz. Functionally graded ceramics were also fabricated with $5 \leq \varepsilon_r \leq 24$. To illustrate the potential of these cold sintered composites to create new substrates and device architecture, a dielectric graded radial index lens was designed and simulated based on the range of $\varepsilon_r$ facilitated by the NBMO-LMO system, which suggested a 78% aperture efficiency at 34 GHz.

**KEYWORDS:** Cold sintering, Microwave dielectric, Na$_{0.5}$Bi$_{0.5}$MoO$_4$, Li$_2$MoO$_4$
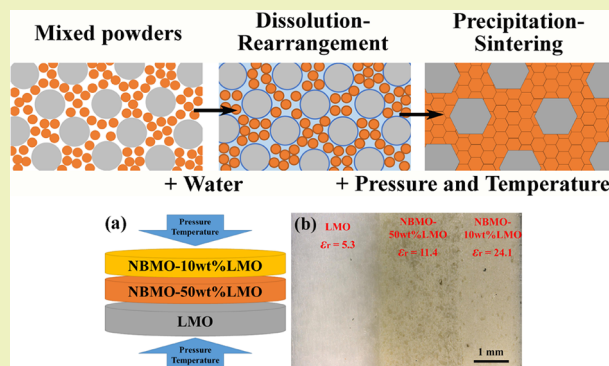
## INTRODUCTION

Microwave (MW) dielectric ceramics are widely used in modern wireless communication systems in applications such as resonators, filters and capacitors.[1] To meet the requirement of miniaturization and reliability of microwave devices, low/ultralow temperature ceramics have attracted interest due to their compatibility with low cost electrodes such as Ag, Cu and Al.[2−6] Typically, MW ceramics not only require a higher permittivity, $15 < \varepsilon_r < 100$, and a large MW quality factor ($Q \times f > 5000$) depending on the application but also a near-zero temperature coefficient of resonant frequency (TCF).[7−12]

Recently, the cold sintering process (CSP) has been shown to have a great potential to achieve dense ceramics/composites/devices at <200 °C.[13−17] Kahari et al. reported Li$_2$MoO$_4$ (LMO) ceramics could be prepared at room temperature by the addition of water and pressure to the LMO powders with $\varepsilon_r$ and $Q \times f$ values comparable with those prepared by conventional sintering method.[13] CSP has also been extensively studied by Guo et al., and successfully applied to many different microwave materials and devices, including LMO, Na$_2$Mo$_2$O$_7$, K$_2$Mo$_2$O$_7$, (LiBi)$_{0.5}$MoO$_4$ and LMO-xPTFE composites.[14−16] More recently, Induja et al. found that Al$_2$SiO$_5$ ceramics could be easily densified using CSP with the help of NaCl.[17]

Although there are several low temperature ceramics fabricated through conventional sintering with near zero TCF,[7−11] no cold sintered materials have been shown to be temperature stable. In this work, Na$_{0.5}$Bi$_{0.5}$MoO$_4$ (NBMO, +43 ppm/°C) and Li$_2$MoO$_4$ (LMO, −160 ppm/°C) ceramics are selected as end-members in a composite series, predicted to achieve zero TCF.[4,18] NBMO-LMO composite ceramics were fabricated using cold sintering and their microwave dielectric properties adjusted continuously as a function of the weight fraction of LMO to achieve zero TCF. The potential use of such ceramics for the fabrication of novel RF substrates and a graded radial index (GRIN) dielectric lens is demonstrated.

## EXPERIMENTAL SECTION

Na$_{0.5}$Bi$_{0.5}$MoO$_4$-xLi$_2$MoO$_4$ composite ceramics (NBMO-xLMO, x = 0, 10, 20, 50, 80 and 100 wt %) were prepared by cold sintering. NBMO powder was synthesized by the solid-state reaction method. Raw materials, Bi$_2$O$_3$ (99.9%, Acros Organics), MoO$_3$ (99+%, Acros Organics) and Na$_2$CO$_3$ (99.9%, Fisher Scientific) were batched stoichiometrically according to the nominal compositions and planetary ball-milled in isopropanol for 4 h. The dried mixed powders were calcined at 600 °C for 4 h to synthesize the compound and then planetary ball-milled in isopropyl alcohol for a further 4 h. The calcined powders were pressed into pellets and sintered at 760 °C for 2 h to obtain NBMO ceramics. To prepare NBMO-xLMO composite ceramics, NBMO pellets were crushed and mixed with LMO (Alfa Aesar, 99%) powder with the addition of 5−10 wt % deionized water.
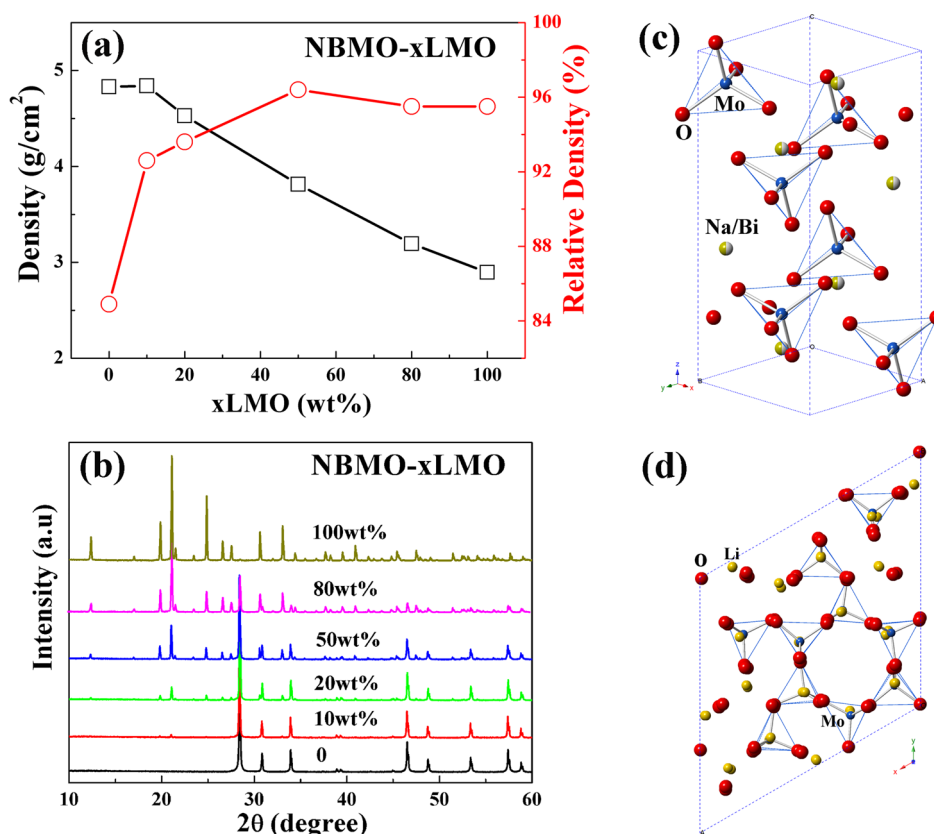
**Figure 1.** (a) Densities and relative densities of NBMO-xLMO composite ceramics; (b) XRD patterns of NBMO-xLMO composite ceramics; schematic crystal structures of (c) NBMO and (d) LMO.

The mixtures were hot-pressed 30 min at 150 °C at 200 MPa and dried 24 h at 120 °C to remove residual moisture.

Bulk densities were obtained from the average results of geometric and Archimedes methods (ethanol as medium). The phase assemblage was studied using X-ray powder diffraction (XRD, D2 Phaser, Bruker) with Cu Kα radiation. Raman spectra were acquired at room temperature by an inVia Raman microscope with a green 514.5 nm laser (Renishaw). Ceramic microstructures were examined using a scanning electron microscope (SEM, Inspect F, FEI) and an optical digital microscope (VHX-5000, KEYENCE). Microwave properties were measured using the $TE_{01\delta}$ dielectric resonator method with a vector network analyzer (R3767CH, Advantest Corporation, Tokyo, Japan). A Peltier device was used to heat the cavity to measure the resonant frequency ($f$) from 25 to 85 °C. The temperature coefficient of resonant frequency (TCF) was calculated with the following formula:

$$\mathrm{TCF} = \frac{f_T - f_{T_0}}{f_{T_0} \times (T - T_0)} \times 10^6 \tag{1}$$

where the $f_T$ and $f_{T_0}$ were the $TE_{01\delta}$ resonant frequencies at temperature $T$ and $T_0$, respectively.

### ■ RESULTS AND DISCUSSION

The densities and relative densities of NBMO-xLMO composite ceramics are shown in Figure 1a. Densities decrease linearly with increasing LMO fraction, due to the lower theoretical density of LMO compare to NBMO (5.68 g/cm³ for NBMO and 3.04 g/cm³ for LMO in this work).[4,18] The relative densities of all the NBMO-xLMO ceramics are in the range of 92.6%–96.4% (except pure NBMO), confirming that dense NBMO-xLMO composites may be made by cold sintering. The room temperature XRD patterns of NBMO-xLMO composite

ceramics from 10° to 60° 2θ are shown in Figure 1b. NBMO crystallizes in a $CaMoO_4$-type Scheelite tetragonal structure with a space-group $I4_1/a$.[18,19] The A-site Na⁺ and Bi³⁺ cations are coordinated by 8 oxygen anions, and the B-site cation Mo⁶⁺ is surrounded by 4 oxygen anions forming a tightly bound $MoO_4$ tetrahedra. LMO has a trigonal structure (space group $R\overline{3}$) with tetrahedral coordination formed by the isolated $MoO_4$ tetrahedra.[20,21] The schematic crystal structures of NBMO and LMO are shown in Figure 1c,d, respectively. The intensity of LMO diffraction peaks in XRD traces increases with the weight fraction of LMO. Furthermore, two sets of peaks corresponding to both NBMO and LMO phases are present for all compositions and no second phase peaks, indicating that NBMO and LMO have not reacted.

Rietveld refinements of the composite NBMO-20 wt %LMO was also performed using the GSAS+EXPGUI package,[22,23] where a two phase refinement ($I4_1/a + R\overline{3}$) was used. Good agreement between the observed and calculated patterns is obtained with low values of $R_p$ = 6.4% and $R_{wp}$ = 9.1%, as shown in Figure 2 and Table 1. The weight fraction of NBMO ($I4_1/a$, 76.4 wt %) and LMO ($R\overline{3}$, 23.6 wt %) phases for NBMO-20 wt %LMO (Table 1) is close to the nominal composition.

Backscattered electron (BSE) and SEM images of cold-sintered NBMO-10 wt %LMO and NBMO-80 wt %LMO composites are shown in Figure 3a−d. Dense microstructures are revealed with two discrete phases present in both samples, in agreement with the XRD result (Figure 1b). According to energy dispersive X-ray spectrum (EDS) analysis (Figure 3e,f), the dark and light contrast regions belong to NBMO and LMO phases, respectively. Furthermore, the grain size of LMO (50−
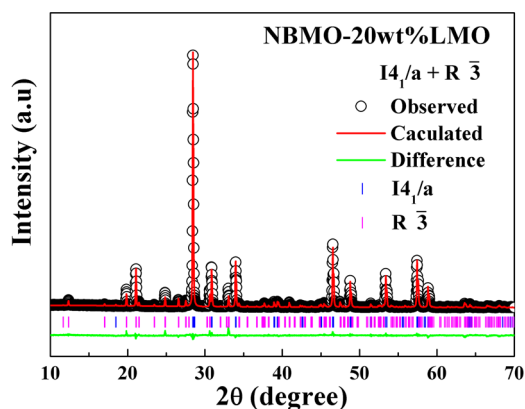
**Figure 2.** Rietveld refinement analysis of NBMO-20 wt %LMO composite ceramic by using the GSAS+EXPGUI package.

100 $\mu$m) is larger than that of NBMO (5−10 $\mu$m), consistent with previous reports.[13,18]

The room temperature Raman spectra of NBMO-xLMO composites in the range of 50−1000 cm$^{-1}$ are shown in Figure 4. Based on the group theory analysis, there are 26 and 82 different vibrational modes for tetragonal NBMO and trigonal LMO,[20,21,24,25] respectively, which are described as follows:

$$\Gamma_{NBMO} = 3A_g + 5B_g + 5E_g + 5A_u + 3B_u + 5E_u \qquad (2)$$

$$\Gamma_{LMO} = 21A_g + 20A_u + 21E_g + 20E_u \qquad (3)$$

For both NBMO and LMO, the even modes $A_g$, $B_g$ and $E_g$ are Raman active, the odd modes $A_u$ and $E_u$ are infrared active, and $B_u$ are inactive vibrations. As a result, there are 13 ($3A_g + 5B_g + 5E_g$) and 42 ($21A_g + 21E_g$) Raman active modes in NBMO and LMO, respectively, as marked in the spectra (partially marked for LMO). Normally, vibrations may be subdivided into internal and external (lattice) modes.[20,21,24,25] Internal modes are related to the vibrations of MoO$_4$ tetrahedra, and the external modes refer to the motions of Bi$^{3+}$/Na$^+$/Li$^+$ cations and the vibrations/translations of MoO$_4$ tetrahedra. For NBMO, the Raman bands above 270 cm$^{-1}$ are internal modes, among which $\nu_1$ and $\nu_3$ represent the stretching motions, and $\nu_2$ and $\nu_4$ represent for the bending motions. The Raman bands below 270 cm$^{-1}$ belong to external modes, among which $E_g$ and $A_g$ close to 190 cm$^{-1}$ are rotational modes, and the others are translational. However, due to the disordered arrangement of Na$^+$ and Bi$^{3+}$ cations, all Raman bands broaden and many overlap, as shown in Figure 4.[25,26] For LMO, the Raman bands above 800 cm$^{-1}$ are attributed to the stretching motions ($\nu_1$ and $\nu_3$) of internal modes. The Raman bands below 85 cm$^{-1}$ belong to translational motions of external modes. Most Raman bands between 85 and 800 cm$^{-1}$ are a mixture of internal and external modes. With the increase of LMO fraction, the intensity of LMO Raman bands increases gradually. It should be noted that several Raman bands belonging to LMO ($A_g \sim 68$ cm$^{-1}$, $\nu_1 \sim 819$ cm$^{-1}$ and $\nu_1/\nu_3 \sim 902$ cm$^{-1}$) are clearly revealed in all NBMO-LMO
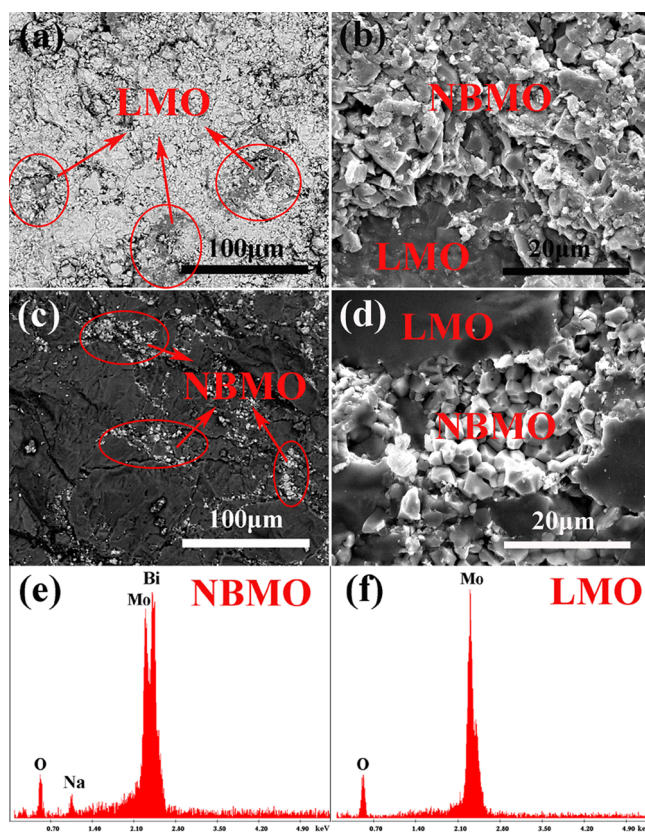


**Figure 3.** BSE and SEM images of cold-sintered (a,b) NBMO-10 wt % LMO and (c,d) NBMO-80 wt %LMO composite samples; the corresponding EDS for both (e) NBMO and (f) LMO phases.
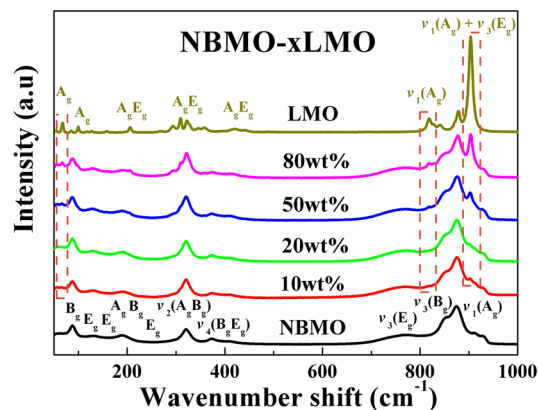


**Figure 4.** Room temperature Raman spectra of NBMO-xLMO composite ceramics.

compositions (except NBMO), further confirming the coexistence of NBMO and LMO phases in the composites.

A schematic illustration of the CSP for NBMO-LMO composites is given in Figure 5.[14−16] NBMO and LMO ceramic powders are initially mixed and then uniformly wetted

**Table 1. Refined Structural Parameters of NBMO-20 wt %LMO Composite Ceramic**

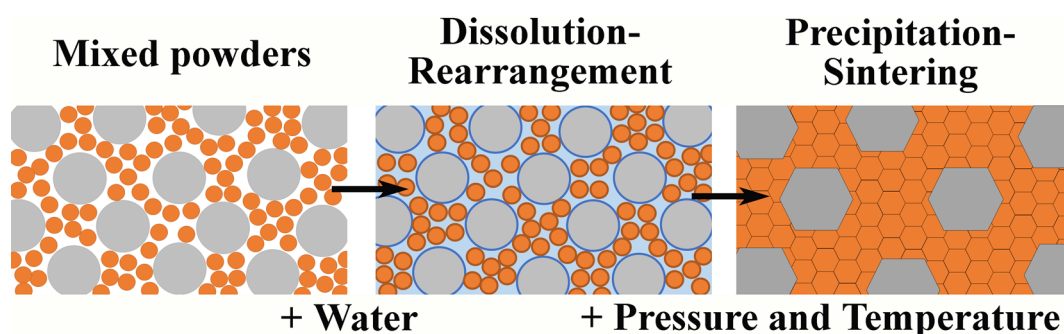| Composition X | Space group | Lattice parameters (Å) | | | Phase fraction (wt %) | R factors (%) | |
| | | a | b | c | | $R_{wp}$ | $R_p$ |
|---|---|---|---|---|---|---|---|
| 20%LMO | $I4_1/a$ | 5.2777 | 5.2777 | 11.5881 | 76.4 | 9.1 | 6.4 |
| | $R\bar{3}$ | 14.3374 | 14.3374 | 9.5884 | 23.6 | | |

**Figure 5.** Schematic illustration of the processing stages for NBMO-LMO composite ceramics (small and large particles are NBMO and LMO, respectively).

with 5−10 wt % deionized water. The solid surface of NBMO and LMO powders decomposes and partially dissolves in the water, leading to the formation of a highly concentrated solution of ions at the particle interfaces. At ∼150 °C and ∼200 MPa, NBMO and LMO particles rearrange themselves mediated by the presence of liquid. The water evaporates and the two phases precipitate at the grain boundaries accompanied by grain growth and a reduction in porosity.

The microwave dielectric properties of NBMO-$x$LMO composites as a function of the wt % LMO are presented in Figure 6 and listed in Table 2. The relative density of cold-



**Figure 6.** Microwave dielectric properties of NBMO-$x$LMO composite ceramics as a function of LMO fraction.

sintered NBMO is as low as 84.9% with $\varepsilon_r$ and $Q \times f$ values of 20.7 and 1500 GHz, much lower than conventionally sintered ceramics, Table 2. Excluding NBMO, the values of $\varepsilon_r$ and TCF decrease linearly from 24.1 and +15.2 ppm/°C for NBMO-10 wt %LMO to 5.3 and −160.3 ppm/°C for LMO. Near-zero TCF (−4.7 ppm/°C) is achieved for NBMO-20 wt %LMO. In contrast to the decrease of $\varepsilon_r$ and TCF, $Q \times f$ increases from 2236 GHz for NBMO-10 wt %LMO to 24319 GHz for LMO, mainly due to the higher $Q \times f$ of LMO with respect to NBMO, as shown in Figure 6c and Table 2.

Assuming no chemical interactions between the respective phases, effective $\varepsilon_r$ in composites may be predicted as follows:[27]

$$\varepsilon^n = V_1\varepsilon_1^n + V_2\varepsilon_2^n (-1 \leq n \leq 1) \tag{4}$$

where $\varepsilon_1$ and $\varepsilon_2$ are the respective permittivities of phase 1 and phase 2; $V_1$ and $V_2$ ($V_1 + V_2 = 1$) are the volume fractions of the corresponding phases. When $n = 1$ or −1, eq 4 becomes a parallel or series mixing law, respectively:

$$\varepsilon = V_1\varepsilon_1 + V_2\varepsilon_2 \tag{5}$$

$$1/\varepsilon = V_1/\varepsilon_1 + V_2/\varepsilon_2 \tag{6}$$

When $n$ approaches 0, Equation 4 becomes logarithmic, usually used for random distributed composites:

$$\varepsilon = \varepsilon_1^{V_1}\varepsilon_2^{V_2}, \text{ i.e., } \lg\varepsilon = V_1\lg\varepsilon_1 + V_2\lg\varepsilon_2 \tag{7}$$

Due to the low density of cold-sintered NBMO, the $\varepsilon_r \sim 34.4$ for normal-sintered NBMO is used in this calculation.[18] As shown in Figure 6a, the measured values of $\varepsilon_r$ for NBMO-LMO composites are within the range of values calculated using Equations 5 and 6, and close to those of Equation 7, indicating that the measured values of $\varepsilon_r$ follow the logarithmic mixing law with the respective weight fraction. TCF and $Q \times f$ may be predicted using the parallel mixing rule,

$$TCF = V_1TCF_1 + V_2TCF_2 \tag{8}$$

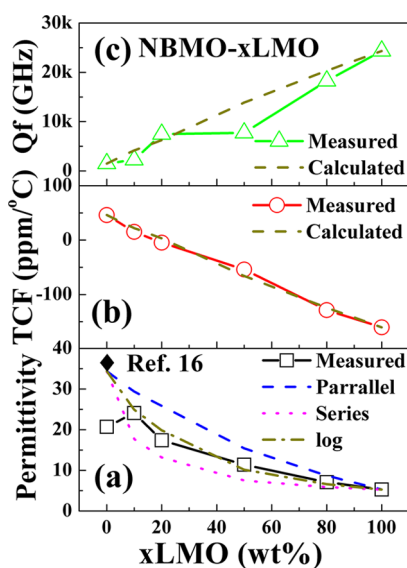**Table 2. Sintering Temperatures, Densities, and Microwave Dielectric Properties of NBMO-$x$LMO Composite Ceramics**

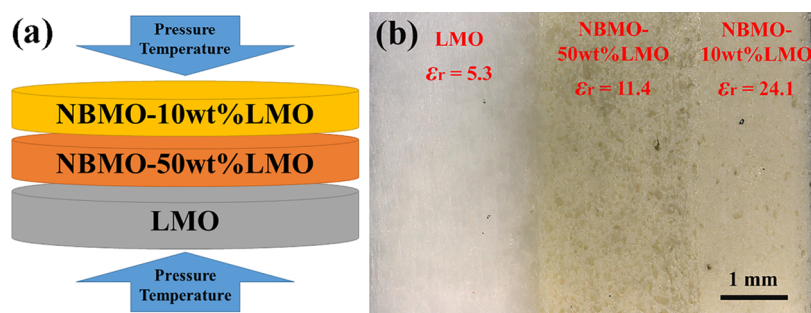| Composition | ST (°C) | $\rho_r$ (%) | $\varepsilon_r$ | tan $\delta$ (%) | $Q \times f$ (GHz) | TCF (ppm/°C) | ref. |
| --- | --- | --- | --- | --- | --- | --- | --- |
| BNMO | 150 | 84.9 | 20.7 | 0.005 | 1500 | +46 | this work |
| 10%LMO | 150 | 92.6 | 24.1 | 0.0018 | 2240 | +15.2 | this work |
| 20%LMO | 150 | 93.6 | 17.4 | 0.0008 | 7470 | −4.7 | this work |
| 50%LMO | 150 | 96.4 | 11.4 | 0.0007 | 7740 | −54 | this work |
| 80%LMO | 150 | 95.5 | 7.1 | 0.0004 | 18250 | −128.7 | this work |
| LMO | 150 | 95.5 | 5.3 | 0.0003 | 24320 | −160.3 | this work |
| BNMO | 690 | | 34.4 | 0.0006 | 12300 | +43 | 16 |
| LMO | 540 | 95.5 | 5.5 | 0.0003 | 46000 | −160 | 4 |

**Figure 7.** (a) Schematic illustration and (b) optical image of three layered composite ceramic.

$$Q \times f = V_1 Q_1 \times f_1 + V_2 Q_2 \times f_2 \qquad (9)$$

where $TCF_1$, $Q_1 \times f_1$ and $TCF_2$, $Q_2 \times f_2$ are corresponding to the TCF and $Q \times f$ values of phase 1 and phase 2, respectively. The measured values of TCF and $Q \times f$ are consistent with those calculated using Equations 8 and 9 (Figure 6b,c), suggesting that the values of TCF and $Q \times f$ can be predicted using simple rules of mixture.

One of key processing advantages of CSP, other than the low temperature, is that there is no lateral shrinkage with dense pellets having the same diameter as the die. Hence, novel macroscopic ceramic—ceramic composites can be fabricated which hitherto would have suffered from inequivalent temperatures and rates of densification during conventional sintering as well as differential thermal expansion on cooling. For higher $\varepsilon_r$ dielectrics, storing energy at resonance is a major problem due to strong reflection at the ceramic surface where there is an abrupt change in $\varepsilon_r$. For planar structures, this can be overcome by multilayering a range of ceramics with different $\varepsilon_r$. Here, three compositions (NBMO-10 wt %LMO, NBMO-50 wt % LMO and LMO) with different $\varepsilon_r$ values (24.1, 11.4 and 5.3) are used to illustrate proof of concept with the fabrication of a three-layered macroscopic ceramic—ceramic composite, Figure 7. Further layers may be introduced to smooth the grading of the composite and give effectively a continuously change in $\varepsilon_r$ as a function of thickness.

Taking advantage of both CSP (low sintering temperature and no lateral shrinkage) and NBMO-LMO (adjustable $\varepsilon_r$), many novel RF applications may be realized including antennas, dielectric lenses, resonators, filters and capacitors. Notably, all ceramic dielectric lenses, able to make use of the high $\varepsilon_r$ of MW ceramics, have proved impossible to fabricate to date due to incompatibility of the sintering of the required dielectrics. A dielectric lens transforms spherical wavefronts that emanate from a feed at the focal point into a planar wavefront. It can also be used to realize highly directed antenna beams. Recently, 3D-printing technology has been used to fabricate GRIN dielectric lenses with locally tailored $\varepsilon_r$[28,29] from polymeric materials such as polylactic acid (PLA) and acrylonitrile butadiene styrene (ABS) which have a low $\varepsilon_r$ (<3) and comparatively high dielectric loss (0.01). In principle, an all ceramic GRIN lens can be fabricated from a series of concentric dielectric cylindrical rings with different $\varepsilon_r$ values. The design principle is shown in Figure 8. The design parameters are given in Table 3 and Table 4. In this work, the dielectric lens is composed of six discrete concentric cylindrical rings. The outermost ring has the lowest $\varepsilon_r$ of 5.3 (pure LMO), whereas the center ring has the highest $\varepsilon_r$ of 24.1 (NBMO-10 wt % LMO). The performance of the lens was simulated using CST Microwave Studio. A $K\alpha$ band (26 to 40 GHz) waveguide
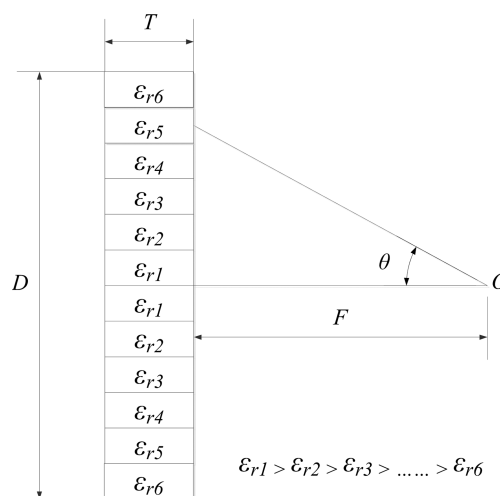


**Figure 8.** Sketch of lens design principle.

**Table 3. Designed Parameters of the GRIN Lens**

| Parameter | Value |
|---|---|
| Diameter ($D$) | 20 mm |
| Focal length ($F$) | 10 mm |
| Thickness ($T$) | 1.35 mm |

**Table 4. $\varepsilon_r$ Values of the Concentric Dielectric Rings**

| Ring no. | $\varepsilon_r$ | Ring outer radius (mm) |
|---|---|---|
| 1 | 24.1 | 2.00 |
| 2 | 20.7 | 4.01 |
| 3 | 17.4 | 5.09 |
| 4 | 11.4 | 7.79 |
| 5 | 7.1 | 8.84 |
| 6 | 5.3 | 10.00 |

(7.112 mm × 3.556 mm) was used in the simulation as the feed to illuminate the lens and the simulated radiation patterns are shown in Figure 9. The simulated results indicate that the directivity is increased by approximately 6 to 8 dB across the frequency range from 26 to 40 GHz by placing the lens at the front of the waveguide at the distance of the focal length, and has approximately 78% aperture efficiency at 34 GHz. The advantage of higher $\varepsilon_r$ is in the miniaturization of these lenses with respect to lower $\varepsilon_r$ glass and polymer systems. In addition, the use of low energy CSP coupled with a simple fabrication route means that for the first time all ceramic dielectric lenses are commercially viable.
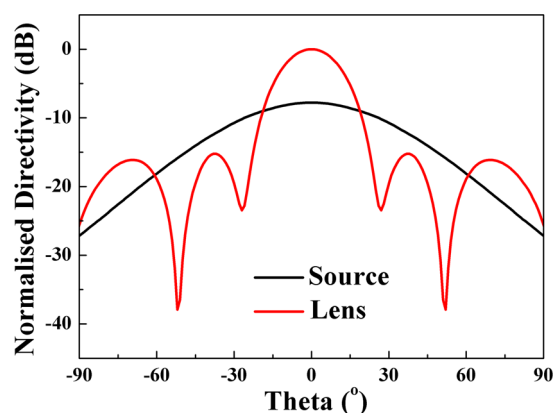
**Figure 9.** Simulated far field radiation patterns of the GRIN lens and source at 34 GHz.

## CONCLUSIONS

NBMO-LMO microwave composite ceramics with densities varying from 92.6% to 96.4% were fabricated by a CSP (150 °C, 30 min and 200 MPa). Both NBMO and LMO phases were found in all the composite ceramics, and there was no evidence of chemical reaction between the two phases within the detection limit of XRD, SEM and Raman spectroscopy. With an increase in weight fraction of LMO TCF and $\varepsilon_r$ decreased from +15.2 ppm/°C and 24.1 for NBMO-10 wt %LMO to −160.3 ppm/°C and 5.3 for LMO, whereas $Q \times f$ values increased from 2236 GHz for NBMO-10 wt %LMO to 24319 GHz for LMO. A near-zero TCF ∼ −4.7 ppm/°C was obtained in NBMO-20 wt %LMO with medium values of $\varepsilon_r$ ∼ 17.4 and $Q \times f$ ∼ 7470 GHz. Graded $\varepsilon_r$ three-layered macroscopic ceramic−ceramic composites were fabricated as proof of concept that the CSP process is ideal for the fabrication of novel RF substrates. A novel dielectric GRIN lens designed and simulated by CST Microwave Studio was presented, which may be fabricated using NBMO-LMO composites, exhibiting 78% aperture efficiency at 34 GHz.

## AUTHOR INFORMATION

**Corresponding Authors**

*D. Wang. E-mail: dawei.wang@sheffield.ac.uk.
*I. M. Reaney. E-mail: i.m.reaney@sheffield.ac.uk.

**ORCID**

Dawei Wang: 0000-0001-6957-2494
Ian M. Reaney: 0000-0003-3893-6544

**Notes**

The authors declare no competing financial interest.
§Currently on secondment from Electronic Materials Research Laboratory, Key Laboratory of the Ministry of Education & International Center for Dielectric Research, Xi'an Jiaotong University, Xi'an 710049, Shaanxi, China

## ACKNOWLEDGMENTS

## REFERENCES

(1) Reaney, I. M.; Iddles, D. Microwave dielectric ceramics for resonators and filters in mobile phone networks. *J. Am. Ceram. Soc.* **2006**, *89*, 2063−2072.

(2) Sebastian, M. T.; Jantunen, H. Low loss dielectric materials for LTCC applications: a review. *Int. Mater. Rev.* **2008**, *53*, 57−90.

(3) Yu, H.; Liu, J.; Zhang, W.; Zhang, S. Ultra-low sintering temperature ceramics for LTCC applications: a review. *J. Mater. Sci.: Mater. Electron.* **2015**, *26*, 9414−9423.

(4) Zhou, D.; Randall, C. A.; Wang, H.; Pang, L. X.; Yao, X. Microwave dielectric ceramics in Li2O-Bi2O3-MoO3 system with ultra-low sintering temperatures. *J. Am. Ceram. Soc.* **2010**, *93*, 1096−1100.

(5) Pang, L. X.; Zhou, D.; Qi, Z. M.; Liu, W. G.; Yue, Z. X.; Reaney, I. M. Structure−property relationships of low sintering temperature scheelite-structured (1-x)BiVO4−xLaNbO4 microwave dielectric ceramics. *J. Mater. Chem. C* **2017**, *5*, 2695−2701.

(6) Sebastian, M. T.; Wang, H.; Jantunen, H. Low temperature co-fired ceramics with ultra-low sintering temperature: A review. *Curr. Opin. Solid State Mater. Sci.* **2016**, *20*, 151−170.

(7) Zhou, D.; Guo, D.; Li, W. B.; Pang, L. X.; Yao, X.; Wang, D. W.; Reaney, I. M. Novel temperature stable high-$\varepsilon r$ microwave dielectrics in the Bi2O3−TiO2−V2O5 system. *J. Mater. Chem. C* **2016**, *4*, 5357−5362.

(8) Zhou, D.; Li, W. B.; Xi, H. H.; Pang, L. X.; Pang, G. S. Phase composition, crystal structure, infrared reflectivity and microwave dielectric properties of temperature stable composite ceramics (scheelite and zircon-type) in BiVO4-YVO4 system. *J. Mater. Chem. C* **2015**, *3*, 2582−2588.

(9) Zhou, D.; Li, J.; Pang, L. X.; Chen, G. H.; Qi, Z. M.; Wang, D. W.; Reaney, I. M. Crystal structure, infrared spectra, and microwave dielectric properties of temperature-stable Zircon-yype (Y,Bi)VO4 solid solution ceramics. *ACS Omega* **2016**, *1*, 963−970.

(10) Ma, J. L.; Fu, Z. F.; Liu, P.; Zhao, L. P.; Guo, B. C. Ultralow-fired Li2Mg3TiO6-Ca0.8Sr0.2TiO3 composite ceramics with temperature stable at microwave frequency. *J. Alloys Compd.* **2017**, *709*, 299−303.

(11) Chen, G. H.; Gu, F. F.; Pan, M.; Yao, L. Q.; Li, M.; Chen, X.; Yang, Y.; Yang, T.; Yuan, C. L.; Zhou, C. R. Microwave dielectric properties of BiVO4/Li0.5Re0.5WO4 (Re = La, Nd) ultra-low firing ceramics. *J. Mater. Sci.: Mater. Electron.* **2015**, *26*, 6511−6517.

(12) Wang, Z. X.; Yuan, C. L.; Yang, T.; Feng, Q.; Liu, F.; Chen, J.; Zhou, C. R.; Chen, G. H. Low-temperature sintering and microwave dielectric properties of Bi0.9Ln0.05Li0.05V0.9Mo0.1O4 (Ln = Sm, Nd and La). *J. Electron. Mater.* **2016**, *45*, 4302−4308.

(13) Kahari, H.; Teirikangas, M.; Juuti, J.; Jantunen, H. Dielectric properties of lithium molybdate ceramic fabricated at room temperature. *J. Am. Ceram. Soc.* **2014**, *97*, 3378−3379.

(14) Guo, J.; Guo, H.; Baker, A. L.; Lanagan, M. T.; Kupp, E. R.; Messing, G. L.; Randall, C. A. Cold sintering: a paradigm shift for processing and integration of ceramics. *Angew. Chem., Int. Ed.* **2016**, *55*, 11457−11461.

(15) Guo, J.; Baker, A. L.; Guo, H.; Lanagan, M. T.; Randall, C. A. Cold sintering process: A new era for ceramic packaging and microwave device development. *J. Am. Ceram. Soc.* **2017**, *100*, 669−677.

(16) Guo, J.; Berbano, S. S.; Guo, H.; Baker, A. L.; Lanagan, M. T.; Randall, C. A. Cold sintering process of composites: bridging the processing temperature gap of ceramic and polymer materials. *Adv. Funct. Mater.* **2016**, *26*, 7115−7121.

(17) Induja, I. J.; Sebastian, M. T. Microwave dielectric properties of mineral sillimanite obtained by conventional and cold sintering process. *J. Eur. Ceram. Soc.* **2017**, *37*, 2143−2147.

(18) Zhou, D.; Randall, C. A.; Pang, L. X.; Wang, H.; Guo, J.; Zhang, G. Q.; Wu, Y.; Guo, K. T.; Shui, L.; Yao, X. Microwave dielectric properties of (ABi)1/2MoO4 (A = Li, Na, K, Rb, Ag) type ceramics with ultra-low firing temperatures. *Mater. Chem. Phys.* **2011**, *129*, 688−692.

(19) Gurmen, E.; Daniels, E.; King, J. S. Crystal structure refinement of SrMoO4, SrWO4, CaMoO4, and BaWO4 by neutron diffraction. *J. Chem. Phys.* **1971**, *55*, 1093−1097.

(20) Barinova, O.; Kirsanova, S.; Sadovskiy, A.; Avetissov, I. Properties of Li2MoO4 single crystals grown by Czochralski technique. *J. Cryst. Growth* **2014**, *401*, 853−856.

(21) Saraiva, G. D.; Paraguassu, W.; Freire, P. T. C.; Ramiro de Castro, A. J.; de Sousa, F. F.; Mendes Filho, J. Temperature induced phase transformations on the Li2MoO4 system studied by Raman spectroscopy. *J. Mol. Struct.* **2017**, *1139*, 119−124.

(22) Larson, C.; Von Dreele, R. B. *General structure analysis system (GSAS)*; Los Alamos National Laboratory Report LAUR; Los Alamos National Laboratory: Los Alamos, NM, 2004.

(23) Toby, H. EXPGUI, a graphical user interface for GSAS. *J. Appl. Crystallogr.* **2001**, *34*, 210−213.

(24) Porto, S. P. S.; Scott, J. F. Raman spectra of CaWo4, SrWo4, CaMoo4, and SrMoo4. *Phys. Rev.* **1967**, *157*, 716−719.

(25) Guo, J.; Zhou, D.; Li, Y.; Shao, T.; Qi, Z. M.; Jin, B. B.; Wang, H. Structure−property relationships of novel microwave dielectric ceramics with low sintering temperatures: (Na0.5xBi0.5xCa1-x)MoO4. *Dalton Trans.* **2014**, *43*, 11888−11896.

(26) Hanuza, J.; Maczka, M.; Macalik, L.; Vandermaas, J. Polarized Raman spectra of NaBi(MoO4)2 crystal and order-disorder effect in solid scheelites. *J. Mol. Struct.* **1994**, *325*, 119−124.

(27) Neelakanta, P. S. *Handbook of electromagnetic materials: Monolithic and composite versions and their applications*; CRC Press: Boca Raton, FL, 1995.

(28) Zhang, S. Design and fabrication of 3D-printed planar Fresnel zone plate lens. *Electron. Lett.* **2016**, *52*, 833−835.

(29) Zhang, S.; Arya, R. K.; Pandey, S.; Vardaxoglou, Y.; Whittow, W.; Mittra, R. 3D-printed planar graded index lenses. *IET Micro. Anten. Propag.* **2016**, *10*, 1411−1419.

G